

RAL 94022

COPY 2 ~~RG~~ ~~RR~~ R3

ACCN: 222430

RAL-94-022

Science and Engineering Research Council

Rutherford Appleton Laboratory

Chilton DIDCOT Oxon OX11 0QX

RAL-94-022

Acceleration of Electrons and Ions by Strong Lower-hybrid Turbulence in Solar Flares

SOLA
ASTR.

R Bingham J J Su V Shapiro et al

March 1994

Science and Engineering Research Council

"The Science and Engineering Research Council does not accept any responsibility for loss or damage arising from the use of information contained in any of its reports or in any communication about its tests or investigations"

ACCELERATION OF ELECTRONS AND IONS BY STRONG LOWER-HYBRID TURBULENCE IN SOLAR FLARES

R Bingham

Rutherford Appleton Laboratory, Chilton, Didcot, Oxon, OX11 0QX

J J Su

National Central University, Chung-Li, Taiwan

V D Shapiro and V Shevchenko

Dept. Electrical and Computer Eng.,

University of California, San Diego, La Jolla, CA 92091

S Ma, and J M Dawson

Dept. of Physics, University of California, Los Angeles CA 90024

K G McClements

AEA Fusion. Culham Laboratory, Abingdon, Oxon OX14 3DB, UK

D S Spicer

Code 930, NASA Center for Computational Sciences, NASA-Goddard Space
Flight Center. Greenbelt, MD 20771

ABSTRACT

One of the outstanding problems in solar flare theory is how to explain the 10-20 keV and greater hard x-ray emissions by a thick target bremsstrahlung model. The model requires the acceleration mechanism to accelerate $\approx 10^{35}$ electrons sec^{-1} with comparable energies, without producing a large return current which persists for long time scales after the beam ceases to exist due to Lenz's law, thereby producing a self-magnetic field of order a few mega-Gauss. In this paper we investigate particle acceleration resulting from the relaxation of unstable ion ring distributions, producing strong wave activity at the lower hybrid frequency. It is shown that strong lower hybrid wave turbulence collapses in configuration space producing density cavities containing intense electrostatic lower hybrid wave

activity. The collapse of these intense nonlinear wavepackets saturate by particle acceleration producing energetic electron and ion tails. There are several mechanisms whereby unstable ion distributions could be formed in the solar atmosphere, including reflection at perpendicular shocks, tearing modes, and loss cone depletion.

Numerical simulations of ion ring relaxation processes, obtained using a $2\frac{1}{2}$ -D fully electromagnetic, relativistic particle in cell code are discussed. We apply the results to the problem of explaining energetic particle production in solar flares. The results show the simultaneous acceleration of both electrons and ions to very high energies: electrons are accelerated to energies in the range 10-500 keV, while ions are accelerated to energies of the order of MeV's, giving rise to x-ray emission and γ -ray emission respectively. Our simulations also show wave generation at the electron cyclotron frequency. We suggest that these waves are the solar millisecond radio spikes. The strong turbulence collapse process leads to a highly filamented plasma producing many localized regions for particle acceleration and resulting in $\approx 10^{17}$ electron "beamlets" of width $\simeq 10\lambda_{De}$ which eliminates the production of large magnetic fields. In this paper we demonstrate that the model produces an energetic electron spectrum with the right flux to account for the hard x-ray observations.

I. INTRODUCTION

In previous papers (McClements et al.[1,2] referred to hereafter as Paper I, and Paper II) we proposed that the acceleration of deka-keV electrons in solar flares could be attributed to lower-hybrid wave turbulence generated by highly anisotropic ion distributions. A particle-in-cell (PIC) simulation code was used to investigate wave activity and electron acceleration resulting from the presence of a dilute population of monoenergetic gyrating ions. We suggested that ion distributions of this type could exist downstream of collisionless perpendicular shocks in the solar atmosphere, pointing out that evidence for the existence of such shocks is provided by type II radio bursts and coronal mass ejections. The ion ring speed in our simulation was about one third of the Alfvén speed, and the ring density was 30% of the total ion density. The initial plasma beta was about 10^{-3} , consistent with conditions in the flaring solar corona. We found that the mean square electron speed parallel to the magnetic field increased by a factor of ten during the simulation, and showed no sign of leveling off (the mean square perpendicular electron speed rose by a much smaller factor). After

600 plasma periods, the flux of deka-keV electrons was already sufficient to produce the hard X-ray emission observed in a typical flare. We concluded that anisotropic ion distributions might be responsible for electron acceleration in flares, via the intermediate process of lower-hybrid wave generation. It is important to point out that any comprehensive model of particle acceleration in flares must explain the apparently *simultaneous* acceleration of electrons to hard X-ray energies and ions to γ -ray energies [3] which was demonstrated in II and below.

Waves with frequencies around the lower-hybrid frequency are likely to be excited whenever there is a deficiency of ions with small pitch angles, or when ions are drifting perpendicular to the magnetic field: such distributions are found in both laboratory and space plasmas. A velocity space ring distribution, for example, may be created artificially in the presence of magnetic fields by energetic particle injection, or resonant heating by electromagnetic waves [4]. Other mechanisms, which could be relevant to natural plasmas, include ion reflection at perpendicular shocks [5], magnetic reconnection [6,7] and the interaction of a high velocity neutral gas with a magnetized plasma [8]. Naturally occurring ion rings are known to exist downstream of the earth's bow shock [9], in the earth's radiation belts [10] and plasma sheet [11], and in the vicinity of comets [12]. Ion loss cone distributions, which exhibit similar instabilities to ring distributions, also occur in natural magnetic mirror systems, such as auroral field lines [13]. Indeed, anisotropic ions are found in virtually every plasma which is accessible to *in situ* measurements.

A number of different wave modes can be excited by ring or loss cone distributions. Parallel-propagating ion cyclotron waves are excited at frequencies below the ion gyrofrequency: in this limit, the ring and background ions are "magnetized", in the sense that there is at least one Larmor orbit in one wave period. Lower-hybrid waves are excited at frequencies lying between the ion and electron gyrofrequencies, in which case the ions are unmagnetized and the electrons magnetized. Ion acoustic-like instabilities also exist, but these are only possible if the electron temperature is significantly greater than the ion temperature or if there is a relative drift between electrons and ions [14]. The linear theory of wave generation by ion ring distributions has been summarized by Mikhailovskii [15], while the quasi-linear theory of the loss cone instability has been treated by Galeev [16]. A unified formalism of the parametric (i.e. nonlinear) instabilities associated with lower-hybrid waves has been developed by Tripathi, Gre-

bogi and Liu [17], who dealt primarily with three wave decay processes and nonlinear ion or electron Landau damping associated with a pump wave near the lower-hybrid frequency. Tripathi et al.[17] were concerned with radio frequency heating of tokamaks, but their analysis can also be applied to situations in which the lower-hybrid mode is generated *in situ* by an unstable ion distribution.

In a strongly turbulent plasma, the modulational instability may cause a lower-hybrid wave to collapse. Normally, the lower-hybrid instability results in the generation of waves in the region of wavevector space where dissipation (i.e. Landau damping) is negligible: this, in fact, is a prerequisite for wave growth. The modulational instability, however, causes waves to cascade to shorter wavelengths, leading to wave collapse and subsequently particle energization by Landau and transit time damping. As a result of wave collapse, direct energy transfer to both electrons and ions can take place.

In this paper we use a PIC code to investigate the acceleration process outlined above, and we apply the results to the solar flare problem. In Section 2 we suggest various mechanisms whereby ion ring or loss cone distributions might develop in the flaring solar atmosphere. We also summarize the theory of lower-hybrid wave collapse, outlining the process which enables electrons and ions to be simultaneously accelerated. In Section 3 we present simulation results which show the effects of ion ring relaxation on the electron distribution and the background ion distribution. The fluxes of high energy electrons and ions produced in the simulation are computed, and compared with those required to explain flare hard X-ray and γ -ray observations. We also study the power spectrum of waves, and in Section 4 we consider the possible relevance of this to solar millisecond radio spike emission. Our conclusions are presented in Section 5.

II. FLARE ACCELERATION MODEL

A. Formation of Ion Ring Distributions

In Paper I we suggested that energetic gyrating ions could be produced in the flaring solar atmosphere by perpendicular shocks, generated by the super-Alfvénic motion of magnetic flux tubes emerging from the photosphere. We showed that such flux tubes could dissipate energy at a sufficient rate to power the impulsive phase of one particular flare. It should be stressed however, that the validity of the results presented in Papers I

and II do not rely on the existence of perpendicular shocks: it is possible that ions rings could also result from magnetic reconnection, which is generally assumed to be the primary mechanism of energy release in flares. Simulations by Leboeuf, Tajima and Dawson [6] have shown that tearing modes produce cross field ion drifts, and Smith [18] has pointed out that fast tearing mode reconnection of the poloidal field in a coronal loop can cause ions to drift across the (much larger) toroidal field. In the case of the slow tearing modes, Arion [19] has shown that bulk ion kinetic energy constitutes about 47% of the total energy released. Ma [20] has carried out full particle in cell simulations of the tearing instability and confirmed the generation of ion ring like velocity distributions.

Processes involved in magnetic reconnection are best illustrated with the magnetic neutral sheet configuration, where an infinite current sheet is centered at $x = 0$, generating oppositely directed magnetic field lines on either side. This configuration is stable against ideal MHD perturbations. However, in the vicinity of $x = 0$ where the \mathbf{B} field vanishes, resistive dissipation, electron inertia, and anomalous dissipation due to plasma collective interactions become important, giving rise to a tearing instability in a boundary layer in which magnetic flux tubes on one side of the neutral sheet can tear, diffuse and connect to those on the other side. The growth rate of the tearing instability is governed by the detailed mechanism of dissipation. Resistive dissipation gives rise to a slow tearing, while electron inertia gives rise to a fast tearing. As the tearing grows, magnetic islands characterised by X and O points in the magnetic field lines are formed, and an electric field in the z -direction is induced near the X and O points. This \mathbf{E} field then gives rise to an $\mathbf{E} \times \mathbf{B}$ drift that drags particles toward $x = 0$ near an X -point and away from an O -point. When a stationary state is reached as a result of nonlinear coalescence of magnetic islands, cold fluid that bring together the magnetic fields of opposite polarities flow toward the X -point at a fraction of the Alfvén speed, and are accelerated as they go across the neutral region, and flow out at the Alfvén speed along the y -axis toward the adjacent O -points, forming standing shocks [21].

With this magnetic reconnection configuration, a direct particle acceleration mechanism due to the inductive electric field can be identified for a neutral sheet where the ion Larmor radius (using the asymptotic magnetic field strength) is smaller than the sheet dimension. Outside the neutral sheet, the ions are magnetized. As they $\mathbf{E} \times \mathbf{B}$ drift toward the X point, some of them become unmagnetized since the \mathbf{B} field is weaker. As a

particle enters the neutral region, it is accelerated in the z -direction by the inductive \mathbf{E} field [22]. The energy gained by the particle depends on how long it will stay in the neutral region before it gets out to be re-magnetized. Therefore, slow ions are more likely to be accelerated with this mechanism. Also since the electric and acceleration field is in the z -direction, perpendicular to the magnetic field, heating mainly takes place in the perpendicular direction increasing the perpendicular kinetic energy of the particle, as demonstrated in a test-particle study of this mechanism by Moses et al [23].

The ions in a flaring loop could also become anisotropic because of loss cone depletion: if the ions are sufficiently energetic, collisional scattering into the loss cone will be slower than the rate at which ions escape, thus giving rise to a well-defined loss cone distribution. To quantify this statement, we note that the collisional scattering time for a proton of energy ϵ and speed v in a plasma of density n is roughly

$$\tau_c \simeq \frac{m_e}{m_p} \frac{\epsilon^2}{\pi e^4 n v \ln \Lambda}, \quad (1)$$

[24] where m_e, m_p are the electron and proton masses, e is the electron charge, and $\ln \Lambda$ is the Coulomb logarithm. The escape time τ_e is roughly L/v , where L is the loop length, and we find that

$$\frac{\tau_e}{\tau_c} \simeq 0.2 \frac{n_{10} L_8}{\epsilon_2^2}, \quad (2)$$

where n, L and ϵ are normalized to $10^{10} \text{cm}^{-3}, 10^8 \text{cm}$ and 100keV respectively. The speed of 100keV proton is much less than the Alfvén speed in a plasma with $n_{10} \simeq 1$ and a magnetic field $B \simeq 500 \text{G}$ (typical values for a flaring loop), and so such energetic protons could easily result from a primary energy release process involving reconnection [18]. Even if L is greater than 10^8cm , the condition $\tau_e < \tau_c$ is still likely to be satisfied close to the loop footpoints. We conclude that loss cone depletion could indeed give rise to a ring-like ion distribution. It is not possible to measure directly the degree of field convergence in a flare loop, but there is indirect evidence, from the spatial distribution of hard X-ray emission, that magnetic mirroring of deka-keV electrons must take place [25].

B. Lower-hybrid Wave Collapse and Particle Acceleration

Wave collapse, predicted by Zakharov [26] as the nonlinear stage of the modulational instability, plays a dominant role in the dynamics of strong

turbulence. Collapse leads to the explosive-like compression of cavities (regions of high wave energy density from which plasma is expelled by wave pressure). The process of collapse results in the transformation of the wave spectrum to larger wavenumbers, producing small scale structures called cavitons, within which the waves are trapped. These waves are absorbed by resonant particles, and a quasi-steady state is eventually reached in which the pumping of wave energy into the system (e.g. from an unstable ion distribution) is balanced by wave absorption (ie Landau damping). It has been shown that lower-hybrid waves can become modulationally unstable, and eventually collapse [27,28]. The mechanism leading to the modulational instability is the nonlinear coupling of lower-hybrid waves with the much lower frequency quasi-neutral density perturbations of ion acoustic waves. The result is a filamentation of the high frequency field, and the formation of elongated nonlinear wavepackets aligned with the magnetic field, the signature of which is a density depletion.

The modulational instability results in the creation of lower-hybrid wave with $k_{\parallel} \neq 0$, in addition to slowly varying magnetic structures. Waves with $k_{\parallel} \simeq \omega_{th}/3v_e$, where v_e is the electron thermal speed, are efficiently absorbed by resonant electrons in the bulk of the distribution. The same waves have perpendicular wavenumbers $k_{\perp} \simeq k \simeq \omega_{th}/3v_i$, where v_i is the ion thermal speed, and can thus be absorbed by (un-magnetized) bulk ions. As a result, simultaneous acceleration of electrons in the parallel direction and ions in the perpendicular direction can occur. Particle acceleration prevents further growth of the pump lower-hybrid wave, thus causing it to saturate.

We will first consider the linear theory of the modulational instability for a pump wave ϕ_o , where ϕ_o is the electrostatic wave potential, with a frequency close to the lower-hybrid frequency, and polarized in the plane perpendicular to the magnetic field coupled to the two lower-hybrid satellites ϕ^{\pm} referred to as the Stokes⁻ and anti-Stokes⁺ modes such that

$$\mathbf{k}_{\pm} = \mathbf{k}_o \pm \mathbf{k}, \quad (3)$$

\mathbf{k}_o and \mathbf{k} being the initial pump wave and low frequency mode respectively, \mathbf{k}_{\pm} are the satellite modes.

The equations describing the coupling of the high frequency lower-hybrid potential ϕ to the low frequency density perturbation δn are given by Shapiro et al [27,28]

$$-\frac{2i}{\omega_{LH}} \frac{\partial}{\partial t} \Delta \phi - R^2 \Delta^2 \phi + \frac{M}{m} \frac{\omega_{LH}^2}{\omega_{ce}} \phi + \frac{M}{m} \frac{\partial^2 \phi}{\partial z^2} =$$

$$-i \frac{M}{m} \frac{\omega_{LH}}{\omega_{ce} n_o} (\nabla \phi \times \nabla \delta n)_z \quad (4)$$

$$\frac{\partial^2 \delta n}{\partial t^2} - \frac{T_e + T_i}{M} \Delta \delta n = + \frac{i \omega_{pe}^2}{4\pi M \omega_{ce} \omega_{LH}} \Delta (\nabla \phi^* \times \nabla \phi)_z \quad (5)$$

where $\Delta = \frac{\partial^2}{\partial x^2} + \frac{\partial^2}{\partial y^2}$ is the transverse Laplace operator and

$$R = \left(\frac{3T_i}{\omega_{LH}^2 M} + \frac{2T_e}{\omega_{ce}^2 m} \frac{\omega_{pe}^2}{(\omega_{pe}^2 + \omega_{ce}^2)} \right)^{1/2}$$

The nonlinear term in equation (4) namely $\nabla \phi \times \nabla \delta n$ is of a vortex type and it vanishes for perturbations that are one dimensional in the plane perpendicular to the magnetic field ($\frac{\partial}{\partial x} = 0, \frac{\partial}{\partial y} = 0$). In one dimension the resulting nonlinearity is smaller by the factor $\frac{m_i}{m_e}$, the vortex nonlinearity is due to the density variation as a result of the electron drift velocity across the magnetic field given by $v_{De} = -\frac{c}{B^2} (\nabla \phi \times \underline{B}_o)$. Since this drift occurs in the background of the low frequency density inhomogeneity δn due to the low frequency ion acoustic mode, it gives rise to a high frequency density variation in the form

$$n_e \simeq \frac{1}{i \omega_{LH}} \nabla \cdot \delta n v_{De} \quad (6)$$

The nonlinear term that couples the slow mode with the high frequency oscillations in equation (5) is due to the ponderomotive force acting on the electrons. In deriving equations (4) and (5) we have neglected the polarization drift and parallel motion of the electrons and ions. The ratio of these terms to the vortex nonlinearity is of the order of (m/M) , therefore the vortex nonlinearity is the dominant term. It is clear from the nature of $\nabla \phi \times \underline{B}_o$ that at least two plane waves or a standing wave must be considered. Due to the appearance of the vortex type of nonlinearity in both equations (4) and (5) the typical threshold wave amplitude for the modulational instability and collapse is less than the wave amplitudes for the Langmuir modulational instability by the factor (m/M) . Equations (4) and (5) can be regarded as the equivalent Zakharov equations for lower-hybrid collapse.

The dispersion relation describing the modulational instability of a pump wave ϕ_o decaying into two lower-hybrid sidebands ϕ^\pm and a low frequency mode δn defined by the complex amplitudes in the form

$$\phi_o = \phi_o \exp \left(i \left(k_{o\perp} r_\perp - \frac{1}{2} \omega_{LH} k_o^2 R^2 t + \frac{\omega_{pe}^2 \omega_{LH}}{2k_o^2 c^2} t \right) \right) \quad (7)$$

$$\phi^\pm = \phi^\pm \exp \left[i \left((\underline{k}_o \pm \underline{k}) \cdot \underline{r} - \frac{1}{2} \omega_{LH} (\underline{k}_o \pm \underline{k})^2 R^2 t + \frac{\omega_{pe}^2 \omega_{LH}}{2 (\underline{k}_o \pm \underline{k})^2 c^2} t - \frac{M}{m} \frac{k_{\parallel}^2 \omega_{LH} t}{2 (\underline{k}_o \pm \underline{k})^2} \mp \omega t \right) \right] \quad (8)$$

$$\delta n = \frac{1}{2} \delta n \exp i (\underline{k} \cdot \underline{r} - \omega t) + c.c. \quad (9)$$

can be obtained from equations (4) and (5) and has the following form

$$\omega^2 - k^2 \frac{T}{M} = -k_o^2 |\phi_o|^2 \frac{\omega_{pe}^2 [\underline{k} \times \underline{k}_o]_z^2}{8\pi n_o m \omega_{ce}^2} \times \left[\frac{1}{|\underline{k} + \underline{k}_o|^2 (\delta_+ + \omega)} + \frac{1}{|\underline{k} - \underline{k}_o|^2 (\delta_- - \omega)} \right] \quad (10)$$

where

$$\delta_\pm = \frac{1}{2} \omega_{LH} \left[|\underline{k}_o \pm \underline{k}|^2 R^2 - k_o^2 R_o^2 - \frac{\omega_{pe}^2}{|\underline{k}_o \pm \underline{k}|^2 c^2} + \frac{\omega_{pe}^2}{k_o^2 c^2} + \frac{M}{m} \frac{k_{\parallel}^2}{|\underline{k}_o \pm \underline{k}|^2} \right]$$

are the frequency mismatches between the Stokes and anti-Stokes satellites and the pump wave. From equation (10) we see that there is no instability for co-planar wave vectors ie for $\underline{k} \parallel \underline{k}_o$.

Equations (10) can be solved to yield the following threshold value of the pump electric field strength E_o and growth rate γ sufficiently above threshold namely

$$\frac{|E_o|^2}{4\pi n_o T_e} > \frac{m \omega_{ce}^2}{M \omega_{pe}^2} \frac{k^2 + k_o^2}{2k_o^2} \delta_o \quad (11)$$

$$\gamma \approx \omega_{LH} \left(\frac{|E_o|^2}{2\pi n_o T_e} \frac{\omega_{pe}^2}{\omega_{ce}^2} \frac{M}{m} \frac{k_o^2}{k_o^2 + k^2} \right)^{\frac{1}{2}} \quad (12)$$

where

$$\delta_o = \frac{1}{2} \left(k^2 R^2 - \frac{\omega_{pe}^2}{(k_o^2 + k^2) c^2} + \frac{\omega_{pe}^2}{k_o^2 c^2} + \frac{M}{m} \frac{k_{\parallel}^2}{(k_o^2 + k^2)} \right)$$

The instability results in the modulation of the pump intensity with the typical perpendicular and longitudinal space scales, L_{\perp} and L_{\parallel} respectively, being given by

$$L_{\perp} \sim k_{\perp}^{-1} \sim R \left(\frac{4\pi n_o T_e}{|E_o|^2} \frac{m \omega_{ce}^2}{M \omega_{pe}^2} \right)^{\frac{1}{2}} \quad (13)$$

and

$$L_{\parallel} \sim \frac{L_{\perp}^2}{R} \sqrt{\frac{M}{m}} \quad (14)$$

with $L_{\perp} \ll L_{\parallel}$.

The modulation of the electric field intensity results in cavity formation on a time scale $t \sim \gamma^{-1}$ where the growth rate γ is given by equation (12).

Bingham et al. [29] have extended this analysis by showing that the low frequency mode could also be a magnetosonic wave. In this case, strong magnetic field perturbations develop perpendicular to the ambient field, leading finally to wave collapse and the cascading of waves to larger parallel wavenumbers, k_{\parallel} . This also occurs even if the initial lower-hybrid wave has $k_{\parallel} = 0$. Due to the modulational instability, two ‘‘satellite’’ waves are excited. The presence of these satellites causes a modulation of the lower-hybrid wave amplitude. The magnetic field develops fine structure, created by long wavelength, low frequency magnetosonic waves, which parametrically couple the initial lower-hybrid wave to its satellites.

Bingham et al. [29] have shown that the threshold wave level for the instability of lower-hybrid waves modulated by low frequency magnetosonic waves is given by

$$\frac{|E|^2}{8\pi n k_b T_e} = \frac{1}{8\pi} \frac{\omega_{th}^2}{k_o^2 c^2} \frac{m_p}{m_e} \frac{k_{\parallel}^2}{k_o^2} \frac{k_{\perp}}{k_{o\perp}} \frac{B^2}{n k_b T_e} \simeq \frac{1}{\beta_e} \frac{\omega_{th}^2}{k_o^2 c^2}. \quad (15)$$

where β_e is the electron plasma beta, and $k_{o\perp}, k_{\perp}$ are respectively the perpendicular components of the lower-hybrid pump wave and the magnetosonic wave.

Contrary to the Langmuir modulational instability, which develops pancake like structures with $L_{\parallel} \ll L_{\perp}$, ie the plane of the pan-cake is perpendicular to the magnetic field, lower-hybrid cavitons are cigar shaped aligned along the magnetic field.

III. SIMULATIONS RESULTS

Particle simulations were carried out using ISIS, a fully electromagnetic, relativistic particle-in-cell code. There are two space dimensions and three velocity dimensions, with the undisturbed magnetic field B_o lying in the coordinate (x, y) plane: there is a small angle between B_o and the x -axis. The ratio m_p/m_e is taken to be 400. Time and space are measured in units of the electron plasma period $1/\omega_{pe}$ and the plasma skin depth c/ω_{pe}

respectively (ω_{pe} is the electron plasma frequency). In terms of these dimensionless independent variables, Maxwell's equations and the equations of motion are independent of the absolute values of the particle masses. Periodic boundary conditions are imposed, so that no particles are lost from the system. A detailed description of ISIS has been provided by Su [30].

The ion distribution consists of a Maxwellian core and a hot ring perpendicular to the magnetic field:

$$f_i(v_{\parallel}, v_{\perp}) = \frac{n_c}{(2\pi)^{3/2} v_c^3} + \exp\left(-\frac{v_{\parallel}^2 + v_{\perp}^2}{2v_c^2}\right) + \frac{n_r}{4\pi^2 v_r v_c^2} \exp\left(-\frac{v_{\parallel}^2 + (v_{\perp} - v_r)^2}{2v_c^2}\right), \quad (16)$$

where v_r is the ring speed, v_c is the core ion thermal speed, and n_c, n_r are the densities of core ions and ring ions respectively. v_{\parallel} and v_{\perp} are the ion speeds parallel and perpendicular to the magnetic field. The normalization of the ring part of the distribution in equation (16) is only correct if $v_r \gg v_c$. The core ions, ring ions, and electrons are all assigned the same initial temperature. The electron thermal speed v_e is set equal to $0.034c$: with a realistic electron mass, this would correspond to an initial temperature of about $7 \times 10^6 K$. It should be remembered, however, that m_p/m_e is artificially small, and so there is a degree of flexibility in relating a thermal speed to a temperature. If, for example, we assumed a realistic value for the *proton* mass, $v_e = 0.034c$ would imply $T \simeq 3 \times 10^7 K$. In fact, electron temperatures inferred from soft X-ray line ratios during the period immediately prior to impulsive hard X-ray emission are typically found to lie in the range $7 \times 10^6 - 2 \times 10^7 K$ [31]. Our initial electron thermal speed is thus consistent with the observations if we take m_e in the simulation to be anything between one and three times the true electron mass.

The other parameters of the simulation are identical to those assumed in Papers I and II: the density ratio of ring ions to core ions n_r/n_c is taken to be $3/7$, close to density ratios observed in the earth's bow shock [9]; the ring speed is set equal to $20v_c (\equiv v_e)$; and the electron gyrofrequency ω_{ce} is twice ω_{pe} . In terms of the simulation parameters, the Alfvén speed is given by

$$v_a = v_c \frac{\omega_{ce}}{\omega_{pe}} \frac{c}{v_e} \simeq 60v_c, \quad (17)$$

i.e. about three times the ring speed. If the ring were created as a result of ion reflection at a perpendicular shock, v_r would be greater than v_a (cf. Paper 1). Alternatively, if the ring arose from a reconnection process, we would expect v_r to be rather less than v_a [18]. Finally, if the ions are initially isotropic but develop a loss cone distribution, it is reasonable to suppose that a broad range of "ring" velocities will be present, although ions with speeds in excess of v_a are likely to be rapidly scattered into the loss cone by ion cyclotron wave turbulence [32]. The value of v_r/v_a chosen for the simulation is therefore quite reasonable. The chosen number density of ring ions is rather high, but, with a ring speed of $20v_c$, it corresponds to an energy density which is less than 5% of $B^2/8\pi$, and is therefore perfectly consistent with a magnetic origin. The mechanism whereby magnetic field energy is transferred to gyrating ions could involve either shock dissipation or reconnection.

Numerical solutions of equations (4) and (5) have been carried out using a pseudo-spectral code to investigate two and three dimensional collapse Fig. 1(a-d) represents solutions in terms of the lower-hybrid electric field amplitude and density perturbation, figures 1(a-d) represent different times. A full description of the 2 and 3-D simulations are given in reference 28.

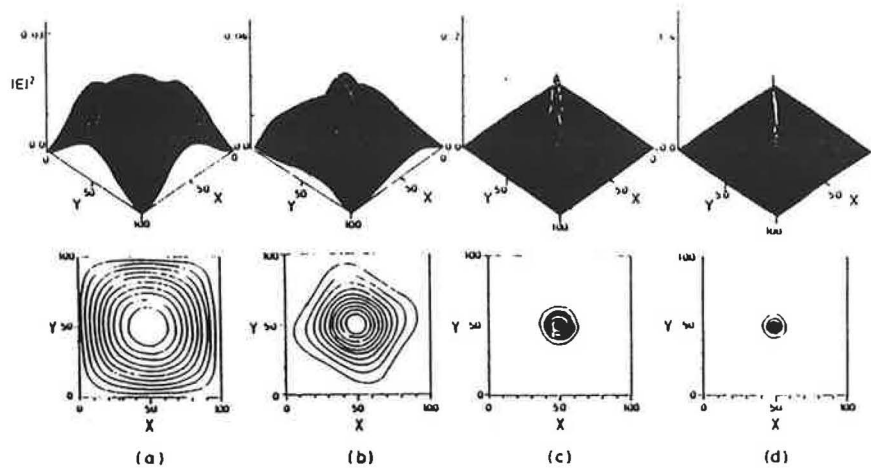


Figure 1. *Dynamics of 2D collapse, spatial structure of electric field and contours of equal densities of the cavity (a) $t = 0. |\delta n|_{MAX} = 0.031$; (b) $t = 230. |\delta n|_{MAX} = 0.06$; (c) $t = 335. |\delta n|_{MAX} = 0.25$; (d) $t = 360. |\delta n|_{MAX} = 0.38$.*

It is clear that the wave energy density increases as the density perturbation decreases. In the 3-D numerical solutions the longitudinal size of the cavities in the z or magnetic field direction is still greater than the transverse scale size. It also appears that it is easier to initialize the collapse processes in 3-D than in 2-D [28]. There is clear evidence from the simulations using ISIS that the acceleration of electrons and ions can be attributed to nonlinear effects associated with density cavitons in the plasma. An analysis of the regions where energetic particles are created, reveals the presence of collapsing wavepackets. These regions also contain intense wave activity as seen in figure 2a,b,c which shows the signature of the modulational instability.

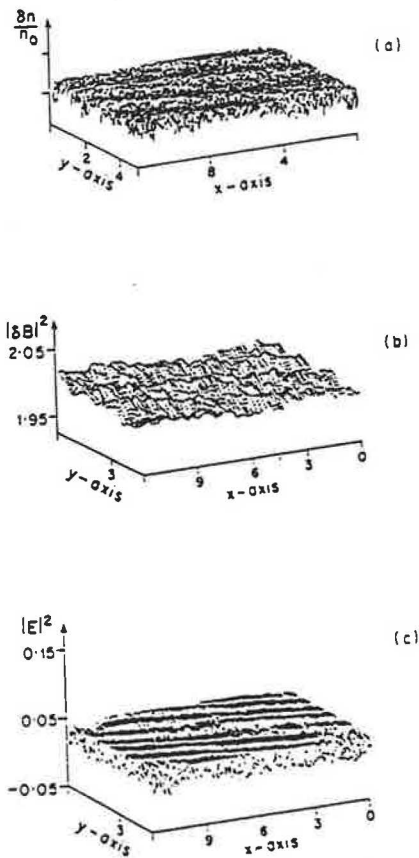


Figure 2a,b,c. *Low frequency density (a) and magnetic field (b). cavitons, arising from the high-frequency electric field envelope (c) Dark regions are regions of most intense waves located in regions of depleted density. x and y are in units of the plasma skin depth, c/ω_{pe} .*

As expected the regions of high wave intensity correspond to regions of low density. These structures are elongated along the magnetic field direction with perpendicular and parallel dimensions of the order of $10\lambda_D$ and $100\lambda_D$ respectively (λ_D being the Debye length). Fig. 3 shows the directions of energetic electrons created within these localized structures showing that the acceleration of electrons is thus highly filamented and field aligned.

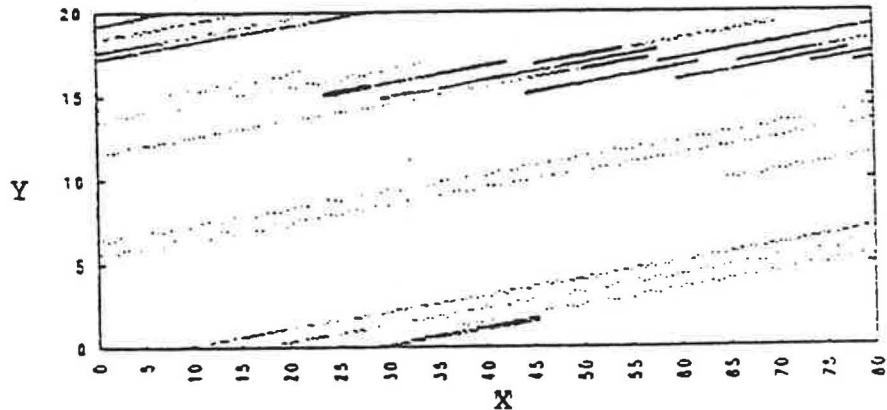


Figure 3. Directions of energetic electrons in x - y plane, showing parallel trajectory and filamentary structure of electrons.

The parallel electron distribution is shown in figure 4 for time corresponding to $t = 300\omega_{pe}^{-1}$, there is a well developed beam which indicates that strong wave particle trapping is taking place within the caviton.

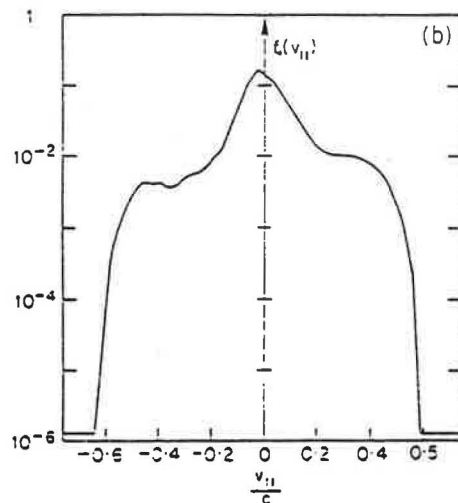


Figure 4. Parallel electron velocity distribution function for time $t = 300\omega_{pe}^{-1}$.

Energetic ions are also observed to originate within the caviton structures and shown in Fig. 5, the final ion distribution is clearly nonthermal consisting of energetic particles in the perpendicular directions some heating and acceleration also occurs in the parallel direction, but to a much lesser extent. Simultaneously to observing energetic electrons and ions intense microwaves are also observed to be generated within these cavitons or hot spots.

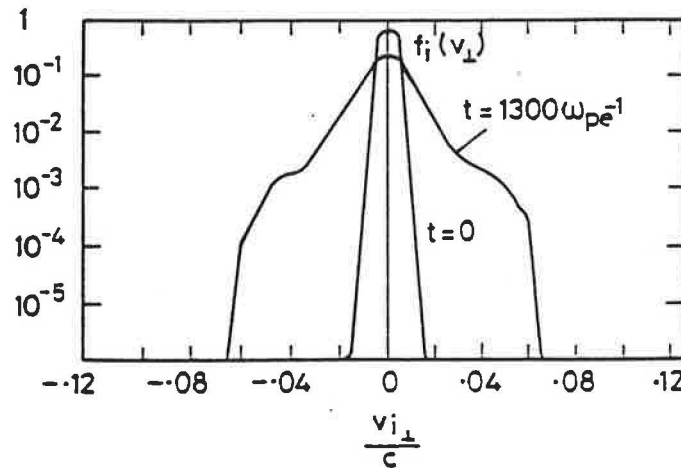


Figure 5. Transverse ion velocity distribution function for times $t = 0$ and $t = 1300\omega_{pe}^{-1}$.

The structure of the cavitons never gets much smaller than about $10\lambda_D$ or one ion gyro-radius, this is in contrast to the fluid theory which predicts collapse down to about λ_D . However, the simulations are fully self-consistent with the damping of the waves playing a major role in the minimum size of the cavitons. The acceleration process inside the cavity cannot be simple quasi-linear diffusion since this would not produce a $+ve$ slope in the electron distribution function. It is probable that the structure acts more like a coherent wave with particles interacting more strongly with the wave through transit time damping or transitional damping. In this case electrons which are in phase with the oscillations inside the structure can gain more energy per interaction than would be allowed with a quasi-linear treatment. The particles are therefore accelerated more effectively than would be expected from the quasi-linear theory. Strong trapping effects may be taking place which can also alter the distributions significantly.

Strong coupling between the particle populations and the waves is taking place inside the cavitons as the wavenumber is decreasing rapidly, coming more into resonance with the bulk of the distribution. This damping is a very effective saturation mechanism which prevents collapse to very small dimensions.

Fig. 6 shows the time evolution of the electric field energy density $|E|^2$, the electron energy, and the ion ring energy, all in dimensionless units. Both the field energy and the electron energy at first increase linearly with time, then grow exponentially in the periods $\omega_{pe}t = 350 - 550$ and $\omega_{pe}t = 1000 - 1300$. At the end of the simulation, we find that approximately 10% of the ring energy has been transferred to the electrons and core ions, while less than 1% of the energy is stored in all the waves generated. The low instantaneous wavelevel is due to strong particle absorption. It can be seen that wave saturation occurs at $\omega_{pe}t \simeq 600$ and $\omega_{pe}t \simeq 1300$.

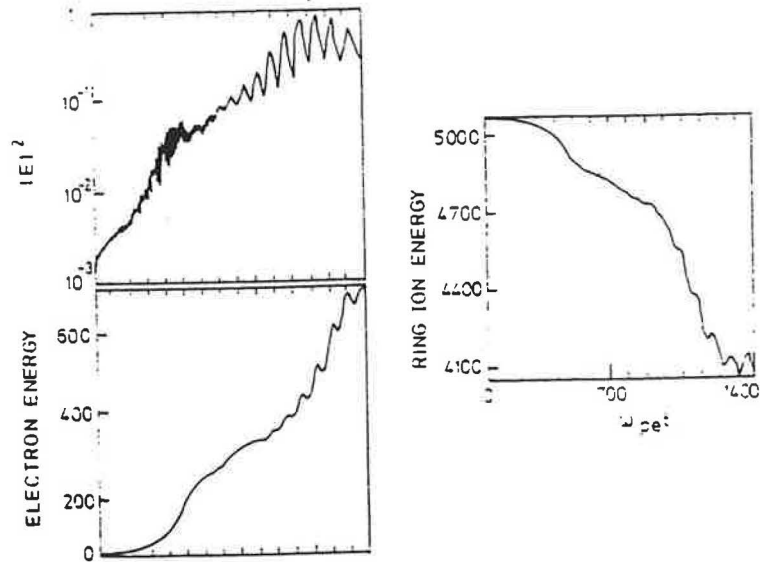


Figure 6. Time evolution of wave energy density, electron energy and ring ion energy up to $\omega_{pe}t = 1500$. Dimensionless energy units are used.

The time evolution of the parallel electron distribution f_e up to $\omega_{pe}t = 1200$ is depicted in Fig. 7. f_e is plotted as a function of the dimensionless parallel momentum $\gamma v_{\parallel}/c$ (γ being the Lorentz factor).

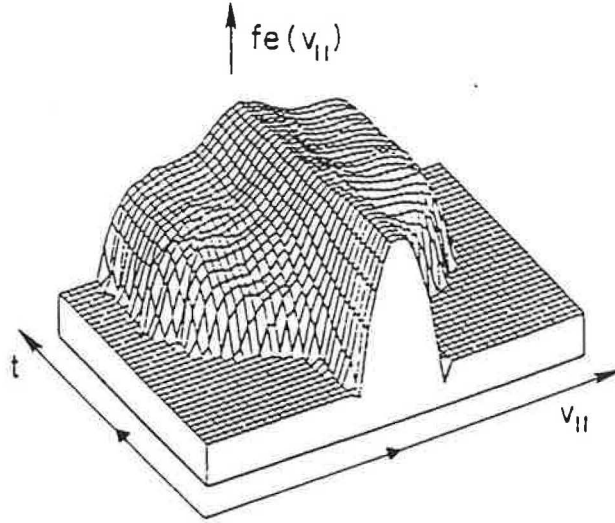


Figure 7. Time evolution of the parallel electron distribution, plotted as a function of $\gamma v_{\parallel}/c$, up to $\omega_{pe}t = 1200$.

The period of exponential wave growth clearly corresponds to the period of rapid electron acceleration. After about $\omega_{pe}t = 600$, the central core of the electron distribution becomes hotter, and the maximum electron speed continues to increase, eventually reaching $0.8c$ at $\omega_{pe}t = 1300$ (corresponding to an energy of $340 - 1000 keV$, depending on the simulation electron mass). From f_e we can compute the rate at which electrons with $\frac{1}{2}m_e v_{\parallel}^2$ greater than ε_o are flowing out of the acceleration site per unit area:

$$F(\varepsilon_o) = 2\pi \int_{\sqrt{2\varepsilon_o/m_e}}^{\infty} v_{\parallel} dv_{\parallel} \int_0^{\infty} v_{\perp} dv_{\perp} f_e(v_{\parallel}, v_{\perp}). \quad (18)$$

$F(\varepsilon_o)$ is plotted for the first 1200 plasma periods of the simulation in Fig. 8. F is normalized to $2\pi n c$. $\varepsilon_o = 20 keV$ is m_e is set equal to its true value. Taking $n = 10^{10} cm^{-3}$, we find that by $\omega_{pe}t \simeq 1200$ the flux has risen to 1.4×10^{18} electrons $cm^{-2}s^{-1}$, considerable higher than the figure obtained in Paper 1. and comparable to the electron fluxes inferred from hard X-ray observations [33]. The time profile of F is similar to that of the electron energy, insofar as the flux increases rapidly during the periods of exponential wave growth.

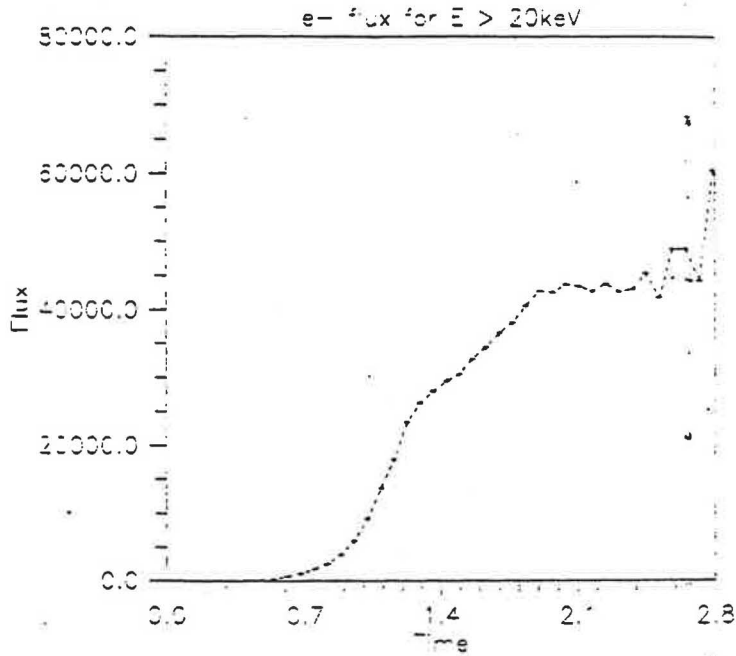


Figure 8. Escaping flux of electrons F with energies above 20keV , up to $\omega_{pe}t = 1200$. The flux is normalized to $2\pi nc$. Thus, if $n = 10^{10}\text{cm}^{-3}$, $F \simeq 1.4 \times 10^{18}$ electrons $\text{cm}^{-2}\text{s}^{-1}$ at $\omega_{pe}t = 1300$.

Fig. 5 shows the distributions of core ions in v_y space at $t = 0$ and $\omega_{pe}t = 1300$. The final distribution is clearly nonthermal, with a mean energy much larger than the initial thermal energy. The distribution of v_z velocities is similar. Some heating and acceleration also occurs in the parallel direction, but to a much lesser extent. If $m_p = 400m_e$, where m_e is the true electron mass, the fastest ions in Fig. 5 have energies of around 450keV (several times the initial energy of the ring ions). If, on the other hand, we set $m_p = 1200m_e$ (consistent with an initial temperature of $2 \times 10^7\text{K}$), we find that a significant number of protons have energies in excess of 1MeV . The energy content of these protons $W(> 1\text{MeV})$ can be estimated crudely from Fig. 5: taking the acceleration volume to be 10^{28}cm^3 (cf. discussion of the April 10 1980 flare in Paper 1), and n to be 10^{10}cm^{-3} , as before, we find that

$$W(> 1\text{MeV}) \simeq 3 \times 10^{30}\text{erg}.$$

Ramaty [34] has estimated W for several γ -ray flares, obtaining figures of between 2×10^{29} erg and 2.5×10^{30} erg. Thus, adopting a value for the initial temperature which is rather high but still consistent with soft X-ray data, we are able to account for the observed fluxes of low energy γ -rays, without having to invoke any additional acceleration. The 1300 plasma periods of the simulation correspond to a time interval of less than a microsecond in the flaring solar corona. As far as the observations are concerned, protons and electrons are therefore accelerated instantaneously and simultaneously: our model can thus provide a natural explanation of the γ -ray and hard X-ray observations presented by Forrest and Chupp [3].

Observations of relativistic solar neutrons [35] indicate that protons must be accelerated in flares to energies in excess of 1 GeV: relativistic protons were not observed in our simulation, and it is possible that a different mechanism must be invoked to account for their production. However, it is reasonable to suppose that the maximum proton speed scales roughly with v_r . Thus, if v_r were set equal to a super-Alfvénic value, appropriate for ion reflection at a perpendicular shock, we would expect to observe proton energies of up to several tens of MeV. Acceleration of ions in the Earth's auroral zone by lower-hybrid waves has been considered in a number of papers by Chang and collaborators [36,37,38], showing general features similar to the present simulation.

The electric field power spectrum at various times during the simulation are shown in Fig. 9. The intense low frequency spikes in (a) and (d) are purely electrostatic, and occur at about twice the lower-hybrid resonance frequency: the fact that emission at this frequency dominates the spectrum early in the simulation indicates the importance of lower-hybrid wave generation in the acceleration process. In the high frequency range, emission occurs predominantly at the electron cyclotron frequency at $\omega_{pe}t \simeq 400$, and close to the upper hybrid frequency $\omega_{uh} = (\omega_{pe}^2 + \omega_{ce}^2)^{1/2}$ at $\omega_{pe}t \simeq 1200$. We have not determined the polarization and propagation direction of these emission features, and so their identification is uncertain. However, the spike $\omega = \omega_{ce}$ has a magnetic component, and it may be the signature of a perpendicular-propagating electromagnetic cyclotron wave [39]. The spike at $\omega = \omega_{uh}$, on the other hand, appears to represent a Bernstein mode.

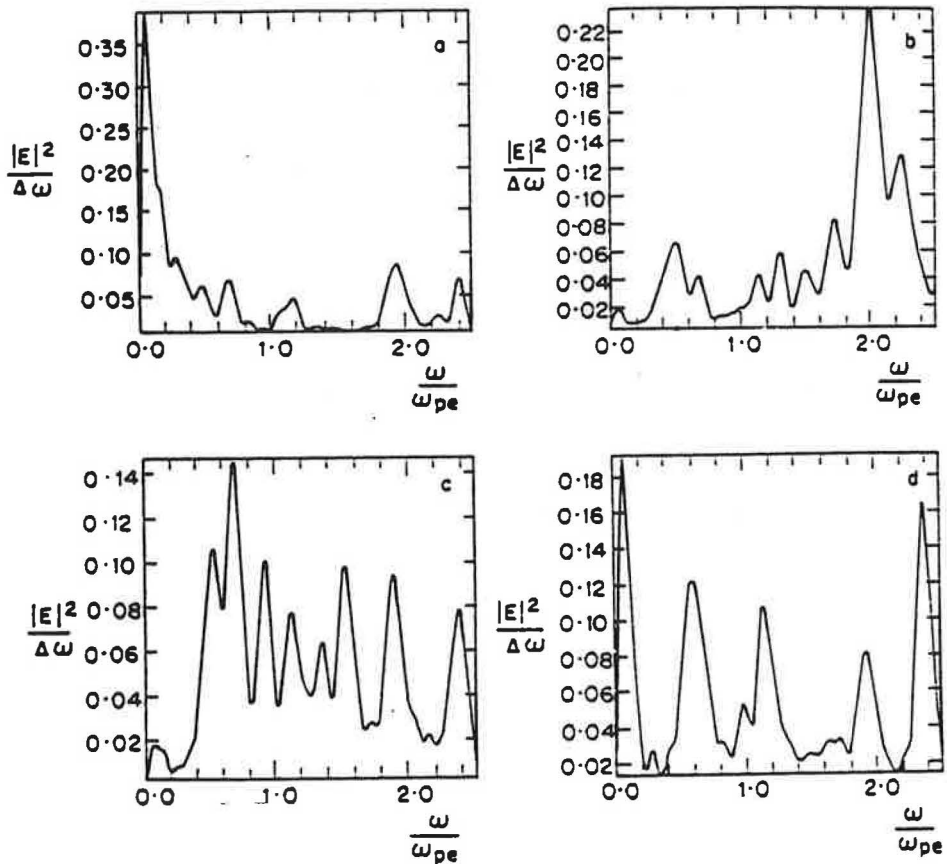


Figure 9. *Electric field power spectrum at $\omega_{pet} = 0.350(a), 400(b), 800(c),$ and $1200(d)$. The intense low frequency spikes in (a) and (d) occur at about the lower hybrid resonance frequency: In the microwave range, emission occurs predominantly at the electron cyclotron frequency at early times, and at the upper hybrid frequency at later times.*

IV. RADIO AND MICROWAVE EMISSION

Our high frequency electric field data can be meaningfully compared with observations of short duration solar decametric and microwave emission ("millisecond spikes"). Slottje [40] obtained the first such observations, inferring full width half maximum durations of less than $20ms$, brightness temperatures in excess of $10^{15}K$, and relative bandwidths $\Delta\omega/\omega$ of less than 0.1. Benz [41] has shown that decametric spikes typically have a rela-

tive half-power bandwidth of 1.5%, although spikes with $\Delta\omega/\omega$ as high as 10% have also been observed [42]. Three examples of narrow bandwidth decametric spike spectra are shown in Fig. 10. A coherent, nonthermal emission mechanism is clearly required to explain these features. Recent observations, for example those presented by Aschwanden and Güdel [43], have shown that decametric spike emission is closely correlated with hard X-ray emission: the radio time profile generally consists of a large number of elementary spikes, modulated by an envelope which lags the hard X-ray burst by typically 2 – 5s.

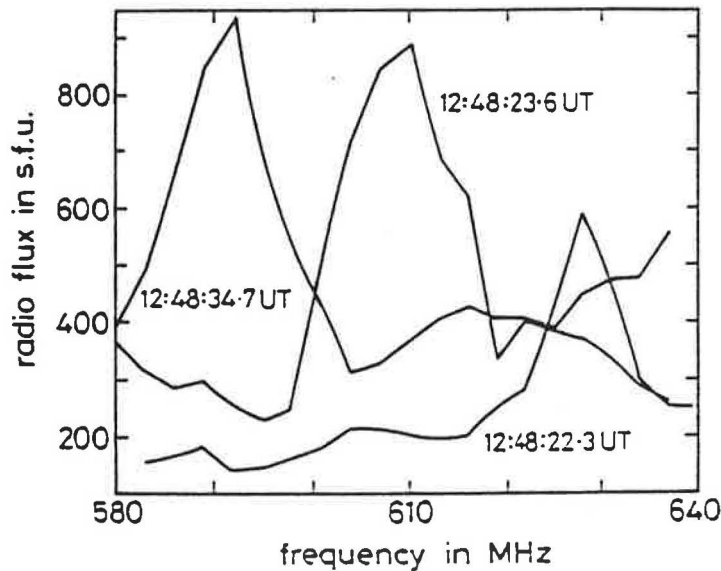


Figure 10. Spectra of three decametric spikes recorded by Benz [41] during the 1980 August 31, 12:48 UT flare. 1 s.f.u. is equal to $10^{-19} \text{ erg cm}^{-2} \text{ Hz}^{-1} \text{ s}^{-1}$.

On the face of it, this last result would seem to imply that spike emission is a secondary process, arising perhaps from the gradual development of a loss cone in the electron distribution, and the consequent generation of cyclotron maser radiation: this, indeed, is the most common interpretation of the data [44]. Aschwanden and Güdel [43], however, have claimed that the apparent time delay between the hard X-ray peak and the peak of the radio spike envelope does not necessarily imply a true delay between the production of energetic electrons (responsible for X-ray emission) and the excitation of a coherent radio signature. The argument used by Aschwanden and Güdel can be summarized as follows. It is logical to assume that the radio emission represents a nonlinear response to the number of

energetic particles $N(t)$ present at any given time in the corona, which is determined by both the acceleration process and the degree of particle trapping (arising from, for example, magnetic mirroring). Denoting the acceleration rate by $S(t)$, we can crudely describe the time development of N by the equation

$$\frac{dN}{dt} = S(t) - \frac{N}{\tau_\ell}, \quad (19)$$

where τ_ℓ is an average loss time, representing the effects of both collisional energy loss and precipitation into the chromosphere. If, following Aschwanden and Güdel, we assume that the radio flux $I_r(t)$ varies as N^2 , we find that

$$I_r(t) \propto \left[\int_{-\infty}^t S(t') \exp \left[-\frac{(t-t')}{\tau_\ell} \right] dt' \right]^2. \quad (20)$$

Aschwanden and Güdel [43] show that this expression predicts a time delay between the maxima of $S(t)$ and $I_r(t)$, which (depending on the value of τ_ℓ and the shape of S) can be comparable to the delay which is observed to occur between the X-rays and the radio spike envelope. Aschwanden and Güdel assume that $S(t)$ is synchronous with the X-ray time profile, $I_x(t)$. The latter will, however, depend to some extent on particle propagation effects, and in fact $I_x(t) \propto N(t)$ if all the X-rays are produced in the corona (unless the coronal plasma density varies on an improbably short timescale). It is likely, however, that the bulk of the hard X-ray emission is produced by electrons precipitating into the relatively dense chromosphere. The lower-hybrid wave model presented in this paper, for example, predicts that electrons are preferentially accelerated along the magnetic field (see e.g. Fig. 3 of Paper 1). Such electrons will mostly lie inside the loss cone, reaching the chromosphere in one loop transit time (typically 0.1s): this is very much less than the time delays found by Aschwanden and Güdel, and so the assumption $I_x(t) \propto S(t)$ could be valid in the context of the present model. In that case, however, τ_ℓ will be approximately equal to the loop transit time, and there will be no significant delays between $I_x(t)$ and $I_r(t)$ (regardless of the radio emission mechanism). It is therefore clear that equation (20) cannot account for the observed delays.

This conclusion is consistent with the analysis of Güdel, Aschwanden and Benz [45] who used a simple kinematic argument to show that the observed delays are too long to be attributable to loss cone formation. They

point out that the spikes associated with a hard X-ray burst are of constant amplitude: modulation of the spike envelope is caused by an increase in the rate of spike occurrence, not spike amplitude, and the hard X-ray flux is proportional to the spike rate. They suggest that the acceleration process is highly fragmented in both space and time, each acceleration site producing one radio spike, and point out that the spike data is characteristic of nonlinear plasma processes which require a threshold and have a well-defined saturation level. This is consistent with the acceleration model outlined in this paper.

One possible qualitative explanation of the hard X-ray/radio spike time delays is the following. Electrons streaming out of the acceleration region may generate high frequency waves via the anomalous Doppler resonance instability [46]. The presence of such waves would enhance the rate of electron pitch angle scattering, thus reducing the flux of electrons reaching the chromosphere. This would have the effect of reducing the overall hard X-ray emission, while the incoherent (Gyrosynchrotron) microwave emission would be enhanced, since it is generated entirely in the corona [47]. At the same time, the total rate at which electrons are accelerated, and hence the flux of coherent microwave radiation associated with the acceleration process, may continue to rise.

The wave data presented in Fig. 9 can be compared with individual solar radio spikes. In particular, the narrow band feature which appears at $\omega \simeq \omega_{ce}$ in Fig. 9 has a full width half maximum bandwidth of less than 0.1. It rises and decays on a timescale of the order of a microsecond. This is very much less than the millisecond timescale of solar radio spikes, but the finite size of the acceleration site and the effects of plasma dispersion mean that the intrinsic lifetime of a microsecond spike is bound to be smeared out by several orders of magnitude. The brightness temperature T_b can be estimated as follows. If the emission is assumed to be isotropic and purely electromagnetic (in the sense that $|\delta B|^2 = |E|^2$, where δB is the magnetic field due to the wave), the equivalent radio brightness is given by

$$B_\nu \equiv \frac{2\nu^2 k_b T_b}{c^2} \sim \frac{c}{4\pi\Delta\nu} \frac{|E|^2}{8\pi}, \quad (21)$$

where $\Delta\nu$ is the spike bandwidth and ν is the spike frequency. Substituting in this expression the appropriate peak value of $|E|^2$ from Fig. 9 (converted to appropriate units), taking ν to be the electron cyclotron frequency (i.e. $\nu = \omega_{pe}/\pi$), and assuming the plasma density to be $10^{10} - 10^{11} \text{ cm}^{-3}$, we obtain

$$T_b \sim 10^{21} K. \quad (22)$$

This is very high compared even to the brightness temperatures found by Slottje [40] and others (brightness temperatures much higher than $10^{15} K$ are also predicted by the cyclotron maser model: see Melrose and Dulk [44]. T_b is difficult to estimate from spike observations, since (for a given radio flux density) it depends on the source size. Sources of spike radiation are too small to be spatially resolved, and their size is estimated by assuming that the spike duration is roughly the transit time of an Alfvén wave or a photon [40], or by assuming that the spike bandwidth is determined by the magnetic field scale length [41]. Such arguments can only yield an upper limit to the source size (typically $10^2 - 10^3 km$), and hence a lower limit of T_b . The true brightness temperatures associated with radio spikes may therefore be considerably greater than those inferred by Slottje [40]. In this context it is worth pointing out that the acceleration mechanism proposed here requires only that energetic gyrating ions extend over a region of space with linear dimensions of the order of $10^3 \lambda_D$, i.e. about $10m$ in the case of the flaring solar corona.

It is possible that radiation at the electron cyclotron frequency cannot escape from the flaring corona, because of gyroresonance absorption, and that the observed millisecond spikes are emitted at higher cyclotron harmonics [44]. Our power spectrum does not extend up to $\omega = 2\omega_{ce}$, but it is reasonable to expect any process which excites waves at ω_{ce} to produce emission at harmonics of ω_{ce} as well. Cyclotron harmonics are likely to have a brightness temperature which is lower than that of the fundamental, and more in line with observations than the figure given by equation (22).

V. CURRENT NEUTRALITY

One of the outstanding problems in solar flare theory is how to explain the 10-20 keV and greater hard X-ray emissions by a thick target bremsstrahlung model. This model requires the acceleration mechanism to accelerate $\approx 10^{35}$ electrons/s with comparable energies, without producing a large return current which persists for long time scales after the beam ceases to exist due to Lenz's Law, thereby producing a self-magnetic field of order a few mega-gauss. The magnitude of the magnetic field produced by the return left after the beam is gone is determined by the resistive diffusion time $\tau \approx 4\pi a^2 \eta c^2$, where η is the resistivity and a the beam

radius. As most models of the beam take as its cross-sectional area the flare kernels, the diffusion time will be quite long, implying mega-gauss magnetic fields persist well past the time the beam ceases to exist. One way around this difficulty is to note that the return current may go unstable to anomalous resistivity mechanisms leading to a dramatic reduction in the diffusion time. However, even with the diffusion time reduced due to anomalous resistivity mega-gauss magnetic fields would exist for short periods of time ($\simeq 10$ seconds) if the beam cross-section area is of order the kernel area. While this is certainly possible observationally (magnetic field strengths cannot be measured in the coronal where one would expect the short lived induced magnetic fields to exist) there are no observational manifestations that such large magnetic are needed to explain (the magnetic pressure resulting from such induced magnetic fields are enormous and should lead to explosions much more violent than are presently observed). The simplest and most self-consistent mechanism for eliminating the production of such large magnetic fields is to reduce dramatically the cross-sectional area of the beam itself and minimize the beam current. This can be accomplished if the actual acceleration mechanism itself generates multiple beams, ie beamlets of small cross-section, the smaller the better since the self-magnetic field produced by the return current, even if it does not 100% neutralize the beam, will be very small in comparison to the pre-existing magnetic field and diffuse away quickly. As this is exactly how the acceleration mechanism discussed in this paper operates there is no problem with this mechanism when it comes to current neutrality and the production of large mega-gauss magnetic fields. To demonstrate this, note that the magnitude of the return current J_R initially is given by

$$J_R = -\frac{J_b}{1 + \left(\frac{\lambda_E}{a}\right)^2}, \quad (23)$$

where J_b is the beam density, a its radius, and λ_E the plasma skin depth, c/ω_{pe} . As our simulation show $a \simeq 10\lambda_{De} = 2\lambda_E$, where λ_{De} is the Debye length.

It therefore follows that $J_R \simeq -\frac{4}{5}J_B$ and complete current neutrality is not achieved. The self-magnetic field associated with the net current is roughly

$$B_\sigma \simeq \frac{2I}{ca}, \quad (24)$$

where $I = \pi a^2 J_{\text{net}}$, $J_{\text{net}} = e\Gamma$, Γ is the beam flux, and $J_{\text{net}} = J_B - J_R = \frac{1}{5}J_B$. Thus

$$B_\sigma \simeq \frac{2}{5}\pi\frac{e}{c}a\Gamma = 2 \times 10^{-20}a\Gamma \quad (25)$$

As the simulations show $\Gamma \sim 10^{18}$ electrons sec^{-1} and $a \simeq 2\lambda_E = 10\text{cm}$ we find $B_\sigma \simeq 0.2$ gauss which lasts for a time ν_*^{-1} , where ν_* is the effective collision frequency. Since ν_* is either the classical collision frequency or greater B_σ will persist for times or order 10^{-2} or shorter. Hence the lifetime of a beamlet and return current system will not be greater than an inverse collision time.

Given that the beam flux for a given ‘‘beamlet’’ is of order $10^{18}/s$ to generate $10^{35}e/s$ our mechanism requires $\approx 10^{17}$ beamlets be present throughout the flare hard X-ray emitting period (note that this does not imply all 10^{17} beamlets exist continuously, but that new beamlets can be formed to replace those whose existence ceases, this is indeed observed in the simulations). We suggest that the origin of these beamlets are due to the collapsing cavitons containing the intense lower-hybrid turbulence, which accelerates the electrons along the magnetic field as shown in Fig. 3. The structure of the cavitons leads naturally to a highly filamented region producing intense electron beamlets.

VI. CONCLUSIONS

We have presented a comprehensive model of particle acceleration in solar flares which can account for the observed hard X-ray and γ -ray emission. We have argued that there are several viable mechanisms whereby unstable (ring-like) ion distributions could be generated: the ubiquitous presence of anisotropic ions in both laboratory and space plasmas suggests very strongly that they will also occur in the atmosphere of the Sun. Ion ring and loss cone distributions can excite waves close to the lower-hybrid resonance frequency. If the lower-hybrid wave amplitude is sufficiently high, the wave becomes modulationally unstable, cascading to shorter wavelengths and Landau damping on parallel-propagating electrons and perpendicular-propagating ions takes place. Lower-hybrid wave collapse can thus, uniquely, lead to the simultaneous acceleration of electrons to deka-keV energies and ions to MeV energies. Particle simulation results show that the relaxation of an ion ring, containing only a small fraction of the magnetic field energy in a flaring loop, can give rise to fluxes of

electrons and ions comparable to those inferred from hard X-ray and γ -ray observations. Furthermore, the accelerated electrons produce bursts of high frequency wave emission close to the electron cyclotron frequency, with narrow bandwidths and brightness temperatures which are much higher than those inferred from millisecond radio spikes. Unlike the electron cyclotron maser instability, which is driven by a loss cone-type anisotropy, these waves are driven by an electron distribution with a nonthermal tail along the parallel direction. In a future paper we intend to study this instability in more detail, identifying in particular the polarization of wave emission at ω_{ce} and its harmonics. This will enable us to carry out a more exact comparison with radio and microwave observations.

ACKNOWLEDGEMENTS

This work was supported by NATO grant CGR 910316, NSF grant PHY 91-21052, and EC grant SC1-CT920773. The particle simulations were carried out at the San Diego Duper-computer Center. We would like to thank C N Lashmore-Davies and an anonymous referee for helpful comments.

REFERENCES

- [1] K. G. McClements, J. J. Su, R. Bingham, J. M. Dawson and D. S. Spicer, *Solar Phys.*, **130**, 229 (1990).
- [2] K. G. McClements, J. J. Su, R. Bingham, J. M. Dawson and D. S. Spicer, *ApJ*, **409**, 465 (1993).
- [3] D. J. Forrest, and E. L. Chupp, *Nature*, **305**, 291 (1983).
- [4] C. N. Lashmore-Davies, and R. O. Dendy, *Phys. Fluids B*, **1**, 1565 (1989)
- [5] K. Papadopoulos, *Proc, 1st Internat. School Plasma Ap.*, ESA sp.161 (Noordwijk: ESA), p.313 (1981).
- [6] J. N. Leboeuf, T. Tajima and J. M. Dawson, *Phys. Fluids*. **25**, 784 (1982).
- [7] J. Drake, private communication (1992).

- [8] V. Formisano, A. A. Galeev and R. Z. Sagdeev, *Planet. Space Sci.*, **30**, 491 (1982).
- [9] G. Paschmann, N. Sckopke, S. J. Bame and J. T. Gosling, *Geophys. Res. Letters*, **9**, 881 (1982).
- [10] A. T. Y. Lui, R. W. McEntire, D. G. Sibeck and S. M. Krimigis, *J. Geophys Res.*, **95**, 20839 (1990).
- [11] J. Chen, G. R. Burkhart and C. Y. Huang, *Geophys. Res. Lett*, **17**, 2237 (1990).
- [12] A. D. Johnson, in *Solar and Planetary Plasma Physics*, ed. B. Buti (Singapore: World Scientific), p.209 (1990).
- [13] D. J. Gorney, A. Clarke D. Croley J. Fennell J. Luhmann and P. Mizera J. *Geophys. Res.*, **86**, 83 (1981).
- [14] B. D. Fried, R. W. Gould *Phys. Fluids*, **4**, 139 (1961).
- [15] A. B. Mikhailovskii, *Theory of Plasma Instabilities Vol 1* (New York: Consultants Bureau), (1974).
- [16] A. A. Galeev, *J. Plasma Phys.*, **1**, 104 (1967).
- [17] V. K. Tripathi, C. Grebogi and C. S. Lui *Phys. Fluids*, **20**, 1525 (1977).
- [18] D. F. Smith, *ApJ*, **288**, 801 (1985).
- [19] D. N. Arion, *ApJ*, **277**, 841 (1984).
- [20] S. Ma, private communication (1993).
- [21] H. E. Petschek, in W N Hess (ed), *Physics of Solar Flares*, NASA SP-50, Washington, D.C., p425 (1964).
- [22] T. W. Speiser, *J. Geophys. Res.* **70**, 4219 (1965).
- [23] R. W. Moses, J. M. Finn and K. M. Ling *J. Geophys Res.* **98**, 4013 (1992).
- [24] B. A. Trubnikov, in *Reviews of Plasma Physics Vol 1*, ed. M.A. Leontovich (New York: Consultants Bureau), p.105 (1965).
- [25] K. G. McClements, *A&A*, **258**, 542 (1992).
- [26] V. E. Zakharov. *Soviet Phys. JETP.* **35**. 908 (1972).
- [27] V. D. Shapiro, and V. I. Shevchenko in *Handbook of Plasma Physics Vol 2*. eds. M.N. Rosenbluth and R.Z. Sagdeev (Amsterdam: Elsevier), p.123 (1984).

- [28] V. D. Shapiro, V. I. Shevchenko G. I. Solov'ev V. P. Kalinin R. Bingham R. Z. Sagdeev M. Ashour-Abdalla J. Dawson and J. J. Su. *Phys. Fluids*. **B5**, 3148 (1993).
- [29] R. Bingham, V. D. Shapiro V. N. Tsytovich U. de Angelis M. Gilman and V. I. Shevchenko *Phys. Fluids B*, **3**, 1728 (1991).
- [30] J. J. Su, UCLA Institute of Plasma and Fusion Research Report, PPG-1301 (1989).
- [31] E. Antonucci, A. H. Gabriel L. W. Acton J. L. Culhane J. G. Doyle J. W. Leibacher M. E. Machado L. E. Orwig and C. G. Rapley *Solar Phys.*, **78**, 107 (1982).
- [32] C. F. Kennel, and H. E. Petschek *J. Geophys. Res.*, **71**, 1 (1966).
- [33] A. G. Emslie, and D. Alexander *Solar Phys.*, **110**, 295 (1987).
- [34] R. Ramaty, in *Physics of the Sun Vol 2*, eds. P.A. Sturrock T.E. Holzer D.M. Mihalas and R.K. Ulrich (Dordrecht: Reidel), p.291 (1986).
- [35] E. L. Chupp, D. J. Forrest J. M. Ryan J. Heslin C. Reppin K. Pinkau G. Kanbach E. Rieger and G. N. Share *ApJ*, **263**, L95 (1982).
- [36] T. Chang, and B. Coppi *Geophys. Res. Lett.*, **8**, 1253 (1981).
- [37] J. R. Retterer, T. Chang and J. R. Jasperse *Geophys. Res. Lett.*, **10**, 583 (1983).
- [38] J. M. Retterer, T. Chang and J. R. Jasperse *Geophys. Res. Lett.*, **91**, 1609 (1986).
- [39] A. I. Akhiezer, I. A. Akhiezer R. V. Polovin A. G. Sitenko and K. N. Stepanov *Plasma Electrodynamics Vol 1* (Oxford: Pergamon), (1975).
- [40] C. Slottje, *Nature*, **275**, 520 (1978).
- [41] A. O. Benz, *Solar Phys.*, **96**, 357 (1985).
- [42] M. Stähli, and A. Magun *Solar Phys.*, **104**, 117 (1986).
- [43] M. J. Aschwanden, and M. Güdel *ApJ*, in press (1992).
- [44] D. B. Melrose, and G. A. Dulk *ApJ*, **259**, 844 (1982).
- [45] M. Güdel, M. J. Aschwanden and A. O. Benz *A&A*, **251**, 285 (1991).
- [46] B. B. Kadomtsev, and O. P. Pogutse *Soviet Phys. JETP*, **26**, 1146 (1968).
- [47] G. D. Holman, M. R. Kundu and K. Papadopoulos, *ApJ*, **257**, 354 (1982).

Figure Captions

Figure 1. Dynamics of 2D collapse, spatial structure of electric field and contours of equal densities of the cavity (a) $t = 0$, $|\delta n|_{MAX} = 0.031$; (b) $t = 230$, $|\delta n|_{MAX} = 0.06$; (c) $t = 335$, $|\delta n|_{MAX} = 0.25$; (d) $t = 360$, $|\delta n|_{MAX} = 0.38$;

Figure 2a,b,c Low frequency density (a) and magnetic field (b). cavitons, arising from the high-frequency electric field envelope (c) Dark regions are regions of most intense waves located in regions of depleted density. x and y are in units of the plasma skin depth, c/ω_{pe} .

Figure 3. Directions of energetic electrons in x-y plane, showing parallel trajectory and filamentary structure of electrons.

Figure 4. Parallel electron velocity distribution function for time $t = 300\omega_{pe}^{-1}$.

Figure 5. Transverse ion velocity distribution function for times $t = 0$ and $t = 1300\omega_{pe}^{-1}$.

Figure 6. - Time evolution of wave energy density, electron energy and ring ion energy up to $\omega_{pe}t = 1500$. Dimensionless energy units are used.

Figure 7. - Time evolution of the parallel electron distribution, plotted as a function of $\gamma v_{\parallel}/c$, up to $\omega_{pe}t = 1200$.

Figure 8. Escaping flux of electrons F with energies above $20keV$, up to $\omega_{pe}t = 1200$. The flux is normalized to $2\pi n c$. Thus, if $n = 10^{10}cm^{-3}$, $F \simeq 1.4 \times 10^{18}$ electrons $cm^{-2}s^{-1}$ at $\omega_{pe}t = 1300$.

Figure 9. - Electric field power spectrum at $\omega_{pe}t = 0.350(a)$, $400(b)$, $800(c)$, and $1200(d)$. The intense low frequency spikes in (a) and (d) occur at about the lower hybrid resonance frequency: In the microwave range, emission occurs predominantly at the electron cyclotron frequency at early times, and at the upper hybrid frequency at later times.

Figure 10. - Spectra of three decametric spikes recorded by Benz [41] during the 1980 August 31, 12:48 UT flare. 1 s.f.u. is equal to $10^{-19}ergcm^{-2}Hz^{-1}s^{-1}$.

